



LAWRENCE
LIVERMORE
NATIONAL
LABORATORY

Effect of Island Overlap on ELM Suppression by Resonant Magnetic Perturbations in DIII-D

M. E. Fenstermacher, T. E. Evans, T. H. Osborne, M. J. Schaffer, M. P. Aldan, J. S. deGrassie, P. Gohil, I. Joseph, R. A. Moyer, P. B. Snyder, R. J. Groebner, M. Jakubowski, A. W. Leonard, O. Schmitz

November 9, 2007

Physics of Plasmas

Disclaimer

This document was prepared as an account of work sponsored by an agency of the United States government. Neither the United States government nor Lawrence Livermore National Security, LLC, nor any of their employees makes any warranty, expressed or implied, or assumes any legal liability or responsibility for the accuracy, completeness, or usefulness of any information, apparatus, product, or process disclosed, or represents that its use would not infringe privately owned rights. Reference herein to any specific commercial product, process, or service by trade name, trademark, manufacturer, or otherwise does not necessarily constitute or imply its endorsement, recommendation, or favoring by the United States government or Lawrence Livermore National Security, LLC. The views and opinions of authors expressed herein do not necessarily state or reflect those of the United States government or Lawrence Livermore National Security, LLC, and shall not be used for advertising or product endorsement purposes.

Effect of island overlap on ELM suppression by resonant magnetic perturbations in DIII-D

M.E. Fenstermacher,^{a)} T.E. Evans,^{b)} T.H. Osborne,^{b)} M.J. Schaffer,^{b)} M.P. Aldan,^{c)}
J.S. deGrassie,^{b)} P. Gohil,^{b)} I. Joseph,^{d)} R.A. Moyer,^{d)} P.B. Snyder,^{b)} R.J. Groebner,^{b)}
M. Jakubowski,^{e)} A.W. Leonard,^{b)} O. Schmitz,^{e)} and the DIII-D Team

^{a)}Lawrence Livermore National Laboratory, Livermore, California, USA

^{b)}General Atomics, P.O. Box 85608, San Diego, California, USA

^{c)}University of California-Berkeley, Berkeley, California, USA

^{d)}University of California-San Diego, La Jolla, California, USA

^{e)}Forschengzentrum, Jülich, Germany

Abstract. Recent DIII-D [J.L. Luxon, *et al.*, Nucl. Fusion **43**, 1813 (2003)] experiments show a correlation between the extent of overlap of magnetic islands induced in the edge plasma by perturbation coils and complete suppression of Type-I edge localized modes (ELMs) in plasmas with ITER-like electron pedestal collisionality $\nu_e^* \sim 0.1$, flux surface shape and low edge safety factor ($q_{95} \approx 3.6$). With fixed $n = 3$ resonant magnetic perturbation (RMP) strength, ELM suppression is obtained only in a finite window in the edge safety factor (q_{95}) consistent with maximizing the resonant component of the applied helical field. ELM suppression is obtained over an increasing range of q_{95} by either increasing the $n = 3$ RMP strength, or by adding $n = 1$ perturbations to “fill in” gaps between islands across the edge plasma. The suppression of Type-I ELMs correlates with a minimum width of the edge region having magnetic islands with Chirikov parameter >1.0 , based on vacuum calculations of RMP mode components excluding the plasma response or rotational shielding. The fraction of vacuum magnetic field lines that are lost from the plasma, with connection length to the divertor targets comparable to an electron-ion collisional mean free path, increases throughout the island overlap region in the ELM suppressed case compared with the ELMing case.

PAC Nos.

I. INTRODUCTION

In the high confinement mode (H-mode) tokamak plasmas needed for sufficient energy gain to extrapolate to attractive power producing reactor scenarios, the plasma edge produces bursts of particles and energy, due to MHD instabilities driven by the steep H-mode edge pressure and current gradients, that are large enough to produce significant erosion of plasma material interaction surfaces [1]. These edge localized modes (ELMs) are nonlinear explosive instabilities [2] that can carry on the order of 20% of the edge pedestal stored energy from the closed, well confined flux surfaces onto open field lines that intersect material surfaces [3]. Extrapolations of ELMs to ITER [4] indicate that the fractional energy loss that can be tolerated without excessive erosion of the target surfaces must be reduced to of order 1% of the pedestal plasma stored energy [5]. The viability of future tokamak reactors operating in H-mode requires techniques to produce at least this factor of 20 reduction in the magnitude of the ELM heat and particle fluxes compared with present experiments while retaining the high energy confinement of the core plasma.

This paper presents physics analysis of plasmas with a lower single-null (LSN) ITER similar shape (ISS) and pedestal electron collisionality [49] similar to ITER, $\nu_e^* \sim 0.1$, in which resonant magnetic perturbations (RMPs) within the H-mode plasma edge, from currents in external perturbation coils, produce at least the required reduction in Type-I ELM [6,7] magnitude needed for projections to future devices. Application of RMPs is just one of many techniques under investigation for ELM control including pellet ELM pacing by the ASDEX-U group [8], ELM pacing using temporal magnetic triggering by the TCV [9] and ASDEX-U [10] groups, various small ELM regimes at JT60-U [11],

ASDEX-U [12], NSTX [13,14], JET [15], C-Mod [16], JFT-2M [17], and DIII-D [18], and ELM-free operation in QH-mode [19-23]. Pioneering work on the effect of edge stochastic fields in circular limited plasmas was done by the TEXT group [24-28], by the Tore-Supra group [29,30] and references therein] and by the TEXTOR group [31-33]. Summaries of work on stochastic magnetic fields in fusion devices can be found in Refs [34] and [35]. There is also recent work with $n = 1$ RMP fields at JET [36]. The recent DIII-D experiments achieved complete suppression of Type-I ELMs at low collisionality in the ISS configuration for a range of plasma conditions [37,38]. ELM suppression was also seen previously in low collisionality plasmas with a lower triangularity shape [39-42] and in higher collisionality plasmas with a more nearly double-null shape [44-47]. The present experiments extend the range of parameter scans, in particular in combinations of $n = 3$ RMPs with applied $n = 1$ fields, in an attempt to test a simple picture of the dependence of ELM suppression on the degree of magnetic island overlap in the plasma edge.

The paper is organized as follows. A description of the experimental conditions and parameter scans is given in Sec. II. The experimental results are given in Sec. III in the context of both the peeling-ballooning stability analysis of the ELMs [48] and a simple picture in which the width of the region with good overlap of magnetic islands in the edge plasma, produced by the RMP coil currents, correlates with the achievement of the necessary reduction in ELM magnitude. In these experiments, the region of island overlap was changed by varying a number of different factors including the strength of the applied perturbation fields and the magnetic geometry in the edge plasma. A discussion of the experimental results including a comparison with theoretical

expectations is given in Sec. IV. Conclusions and plans for future studies are presented in Sec. V.

II. DESCRIPTION OF EXPERIMENTS

For the experiments reported in this paper the plasmas had an ISS and divertor pumping to control the plasma density so that the pedestal electron collisionality, $\nu_e^* \sim 0.1$ was close to the value expected in ITER. Since the edge stability has a strong dependence on both shape and collisionality (through the bootstrap current) the interpretation of the applicability of the RMP ELM suppression technique to ITER is more straightforward with these two parameters matched to the ITER values. The 2D equilibrium reconstruction of an ISS plasma [Fig. 1(a)] shows that the outer strike-point is in the optimal pumping position for good density control using the DIII-D lower outer cryopump, with lower triangularity $\delta_{\text{lower}} = 0.67$, upper triangularity $\delta_{\text{upper}} = 0.33$, and elongation $\kappa = 1.8$. For reference, the ITER shape parameters are $\delta_{\text{lower}} = 0.67$, $\delta_{\text{upper}} = 0.33$, and $\kappa = 1.8$. The ISS plasmas were typically run with plasma current $I_p = 1.65$ MA, toroidal field $B_T = 1.9$ T (with scans in the range $I_p = 1.4$ – 1.7 MA and $B_T = 1.75$ – 2.10 T) and injected neutral beam power $P_{\text{inj}} = 7$ – 10 MW giving normalized beta $\beta_N = \beta / (I_p / a B_T)$ 1.7–2.4, where a is the minor radius of the plasma and β is the ratio of plasma pressure to magnetic field pressure. Time histories of a typical discharge (Fig. 2) show the suppression of the Type-I ELMs within 600 ms after the $n = 3$ RMP from the I-coil is turned on, similar to results obtained with a lower triangularity shape [39–42].

The spectrum of helical magnetic field perturbations used in these experiments included $n = 3$ components from the DIII-D internal coil (I-coil), $n = 1$ components from the DIII-D external error field correction coil (C-coil) and residual $n = 1, 2$ and 3 field errors from the DIII-D equilibrium field coils. The configuration of the coils [Fig. 1(b)]

includes six toroidal C-coils outside the toroidal field (TF) and equilibrium field (EF) coils, and two rows of six I-coils mounted on the inside of the vacuum vessel inside both the TF and EF coils. The I-coils for these experiments were configured for $n = 3$ and the C-coils were configured for $n = 1$ helicity. The I-coils can be configured for even up/down parity with upper and lower pairs having current in the same direction or odd parity with currents in the opposite direction. As described in detail in the following sections, the effectiveness of the helical field perturbations in ELM suppression appears to be correlated with the radial extent of the region in which the magnetic islands produced by the field perturbations overlap. The calculation of the extent of the island overlap region is done with the SURFMN code [50]. This is a vacuum fields calculation that does not include the plasma response or rotational shielding effects. For $n=3$ even parity, Fig. 3 shows a typical poloidal mode spectrum calculated by SURFMN for discharges used in these experiments. Best ELM suppression is typically obtained when the peak in the mode spectrum is pitch aligned with the safety factor in the edge plasma, as in the example of Fig. 3 where $m = -nq(\Psi)$ is aligned with the local maximum in the mode spectrum from the separatrix well into the core plasma ($\Psi_N \sim 0.5$). Calculations of the location and widths of the resulting islands (Fig. 4) during the ELM suppressed phase of the discharge in Fig. 2 show that the islands are well overlapped in a region of the plasma edge that is significantly wider than the edge pressure pedestal. For discussion of magnetic island overlap it is useful to introduce the Chirikov parameter [51]. This parameter is defined, for any adjacent pairs of magnetic islands, as the average island width normalized to the inter-island radial spacing. Significant field stochastization is indicated by Chirikov parameter > 1.0 . In the discussion below, the width of the region

for which this criterion is satisfied is obtained from a fit to the radial profile of the Chirikov parameters for each pair of adjacent islands in the edge. This width, denoted by $\Delta_{\text{chir}>1}$, will be used as representative of the width of the island overlap region. In the example of Fig. 4 $\Delta_{\text{chir}>1}/\Delta_{\text{ptot}}^{\text{ped}} = 2.9$ during the ELM suppressed phase of the discharge, where $\Delta_{\text{ptot}}^{\text{ped}}$ is the width of the total pressure profile.

The experiments reported here used five techniques to vary the overlap of the perturbed magnetic islands in the edge plasma, viz. by varying: 1) the I-coil current, i.e., the strength of the applied $n = 3$ RMP, 2) the toroidal field at fixed q_{95} (i.e. $I_p \sim B_T$) and RMP perturbation, 3) the edge plasma density, n_e^{ped} using gas puffing which also affected the edge bootstrap current and magnetic shear, 4) the range of q_{95} values in combination with the up-down parity of the applied $n = 3$ RMP, and 5) the combination of $n = 3$ and $n = 1$ perturbations in q_{95} scans through variation in I_p . In all cases, the basic C-coil current was set by an algorithm that calculates the experimentally determined optimum $n = 1$ error field correction current [52]. The algorithm used a linear combination of two actuators, I_p and the toroidal field coil current, to adjust the C-coil current and phase for empirical correction of field errors due to the toroidal and poloidal equilibrium coils. To vary the mixture of $n = 3$ and $n = 1$ fields, the leading coefficient in the algorithm, “C-coil multiplier,” was increased to add additional $n = 1$ field to the perturbation spectrum in an attempt to “fill-in” regions of the island profile and achieve additional island overlap. Parameters from the various scans are compiled in Table 1.

III. EXPERIMENTAL RESULTS

Linear peeling-ballooning (P-B) stability analysis with the ELITE code [53,54] indicates that in the ISS plasmas, as was the case in lower triangularity plasmas with the ITER pedestal collisionality, application of $n = 3$ RMPs moves the pedestal plasma operating point from the unstable region to the stable region [38,55], resulting in suppression of Type-I ELMs. The linear P-B calculations indicate that the stabilization of the ELMs by the RMPs is due primarily to a reduction of the density and density gradient in the pedestal and the corresponding bootstrap current reduction. Although the location of the stable region in the P-B space parameterized by the pressure gradient and edge current is somewhat different for the ISS plasmas vs lower triangularity discharges (as discussed in Ref. [38]) the interpretation of the stabilization mechanism is consistent in the different shapes.

With fixed plasma shape and safety factor $q \sim B_T/I_p$, parameter scans of: (1) the $n = 3$ RMP from the I-coil, (2) the $n = 3$ perturbation normalized to the toroidal field, $\delta br/B_T$, at fixed I-coil current, and (3) pedestal plasma parameters using gas puffing at fixed I-coil current, all show an initial rapid change of the ELM character and pedestal density at I-coil turn-on with full ELM suppression occurring later in the discharges. Here δbr is the radial perturbation field. Time histories from the I-coil current scan (Fig. 5) at fixed B_T/I_p show that when the I-coil is first turned on there is a reduction of the pedestal density and a change in the ELM character (amplitude and frequency) but full suppression does not occur immediately. ELM suppression does occur progressively earlier in the discharge as I-coil current increases. After the initial rapid decrease at the I-coil turn-on, the pedestal density decreases very slowly during the ELM suppression

phase. The scans of $\delta br/B_T$ at constant I-coil current and constant edge safety factor q_{95} were done by lowering the toroidal field and plasma current together on a shot-to-shot basis. Time histories (Fig. 6) again show an immediate change in ELM character at I-coil turn-on with full suppression occurring later in the discharge. Finally, the scans of pedestal plasma parameters at fixed I-coil current were done by adding a supplemental gas puff from the lower outer SOL region (Fig. 1). Time histories (Fig. 7) show that this achieved a modest variation in pedestal electron density, temperature and pressure.

A simple model, proposing that a minimum width of the edge region with good overlap of the magnetic islands from the RMP is related to the achievement of full ELM suppression, is consistent with observations from the I-coil current, $\delta br/B_T$ and n_e^{ped} scans described above. In each case, multiple time slices at 50 ms intervals were selected from each shot both before and during the I-coil-on phase. For each time slice a comprehensive pedestal profiles analysis [56] was done including the effects of the pedestal impurity profile and fast ion pressure contributions from the beams. The profile analysis for time slices during an ELMing phase used edge Thomson scattering (n_e and T_e) and charge exchange recombination (CER) spectroscopy (T_i , impurity density) data from the period at the end (80%-99%) of the ELM cycles. For each timeslice during the ELMing phase, the profiles were obtained by fitting all the data collected from the end of the ELM cycles for all ELMs in a window (typically 300 ms) centered on the timeslice. Profiles during the ELM suppressed phases were formed from all the data within a 200 ms window centered on the timeslice. In each case a hypothesis that the axisymmetric equilibrium separatrix should be one fourth of the pedestal width outside the point of maximum gradient in the electron temperature profile [57] was used to set

the radial alignment of the profiles with respect to the axisymmetric equilibrium separatrix at the outer midplane. Hyperbolic tangent fits to the pedestal density and temperature profiles were then used in axisymmetric equilibrium reconstruction (“kinetic EFIT”) analysis [58] for each timeslice to calculate the q profile including the effects of the edge bootstrap current. The current density in the H-mode pedestal region was not measured in these experiments. Instead, the flux surface averaged current density used in the equilibrium calculations was set to the sum of the neoclassical bootstrap current, given by the Sauter expression [49], and the fully relaxed ohmic current using neoclassical resistivity.

A complete mode spectrum analysis using the SURFMN code [50], including calculation of the Chirikov parameter profile in the edge, was then done on each kinetic EFIT including the I-coil $n = 3$ perturbation, the $n = 1$ perturbation from the C-coil, and the measured $n = 1, 2$ and 3 error fields in DIII-D [59]. This calculation used only the vacuum fields without any correction for the plasma response, so any effects of screening of the perturbation fields due to plasma rotation are not included here. A spline fit of the Chirikov parameter profile was used to determine the width of the edge region with Chirikov parameter > 1.0 . The scatter plot of ELM amplitude (from a D_α chord viewing the outer divertor leg) as a function of the width in normalized poloidal flux of the edge region with Chirikov parameter > 1 is shown in Fig. 8. All ELMs within a given kinetic EFIT 50 ms time window are plotted with the island overlap width for that window. Although a distribution of ELM amplitudes is observed at all values of the overlap region width, consistent with the non-linear nature of the ELM instability, the data shows that the maximum ELM size is well ordered by this width parameter. Data for widths less

than 0.07 (Fig. 8(a)) are from the phase before I-coil turn-on in which islands in the edge are due only to the applied $n=1$ error correction fields from the C-coil and the intrinsic error fields. An expansion of the plot for the range $0.1 < \Delta_{\text{chir}>1} < 0.25$ is given in Fig. 8(b). The data with widths $0.1 < \Delta_{\text{chir}>1} < 0.165$ are from phases with the I-coil on, including the transient phase immediately after I-coil turn-on, in which ELMs remain. When the vacuum island overlap width $\Delta_{\text{chir}>1} > 0.165$ large Type-I ELMs are suppressed as shown by the reduction in the maximum D_α intensity by at least a factor of 10. The data during the ELMing phase with the I-coil on also suggests decreasing maximum ELM D_α amplitude with increasing vacuum overlap region width.

Scans of the edge safety factor (q_{95} = safety factor at 95% poloidal flux) by variation of the plasma current, I_p , show that complete suppression of ELMs by application of RMPs is a resonant phenomenon that depends sensitively on the q -profile. All of the experiments to date have scanned q_{95} downward throughout the discharge using an upward ramp in the plasma current at fixed B_T . Both of the discharges in (Fig. 9) have 3.0 kA in the I-coil and the nominal error field correction current in the C-coil. Each shows a window in q_{95} for ELM suppression during the I_p ramp; in shot 128470 extended periods of ELM suppression were observed for $3.46 < q_{95} < 3.67$, i.e., $\Delta q_{95} = 0.21$ and in shot 129475 the window for extended periods of ELM suppression was $3.35 < q_{95} < 3.42$ ($\Delta q_{95} = 0.07$). This variation in the resonance window width gives an indication of the dependence on other parameters. For example, in these discharges the initial I_p ramp rate at the beginning of the discharges were slightly different. As a result, the discharges developed significantly different core MHD activity; shot 128470 had a

3/2 tearing mode and shot 128475 showed intermittent levels of 1/1 sawteeth during the time with the I-coil on.

Periods of extremely large reduction in Type-I ELM size and increase in ELM frequency were observed in low collisionality plasmas at $q_{95} \sim 7.5$ using $n = 3$ RMPs that were pitch resonant at high edge- q with the odd parity connection of the upper and lower rows of the I-coils, providing further evidence that ELM suppression using RMPs is a resonance phenomenon. The poloidal mode spectrum plot (Fig. 10) for this case shows good alignment of pitch resonant modes $[m = -nq(\Psi_N)]$ with a local peak in the spectrum in the edge plasma. These plasmas extend to low ITER-like collisionality the results of previous experiments in high collisionality plasmas using odd parity $n = 3$ RMPs from the I-coil [44-48]. In contrast to the present $q_{95} = 7.5$, $\nu_e^* \sim 0.1$ case, the previous $\nu_e^* \sim 1.0$ discharges were run at $q_{95} = 3.7$ and therefore had very little resonant field component. Both the present $q_{95} = 7.5$, $\nu_e^* \sim 0.1$, and the previous $q_{95} = 3.7$, $\nu_e^* \sim 1.0$ cases had high levels of non-resonant helical field perturbations due to the odd parity I-coil connections. In the previous case at high collisionality with odd parity $n = 3$ fields, Type-I ELMs were replaced by very small, very high frequency Type-II ELMs without substantial change in the pedestal parameters [39]. At low collisionality in the recent experiments (Fig. 11), the Type-I ELM size was substantially reduced (factor of 18) and the frequency substantially increased (factor of 4) [39]. Initial analysis of the plasma profiles showed that the pressure and pressure gradient were reduced, primarily due to reductions in the density, as in the low q_{95} even parity I-coil plasmas at low collisionality. However, the ELMs that remained at high q_{95} with odd parity RMP had

lower normalized energy loss ($\Delta W_{\text{ELM}}/W_{\text{PED}}$) than the ELMs before the coil turn-on [39] in addition to the large reduction in absolute energy loss.

The range of q -profiles for which complete ELM suppression is obtained can be expanded by increasing the $n = 3$ perturbation strength or by increasing the contributions of $n = 1$ perturbations to “fill-in” the overlap of the edge islands. Scans to explore the safety factor resonance window for ELM suppression used upward I_p ramps at fixed B_T to produce downward ramps of safety factor (Fig. 12). On a shot-by-shot basis either the current in the I-coil or the current in the C-coil was increased to increase the $n = 3$ or $n = 1$ perturbation fields respectively. Again the data in Fig. 12(f) shows that the first response to the turn-on of RMP fields was a reduction of the pedestal density. In these cases the reduction occurred at significantly higher safety factor ($q_{95} \sim 4.2$) than in the cases of Figs. 5(h), 6(f), and 7(f). The D_α signals show that the ELM size decreased and frequency increased slightly but not as much as at lower q_{95} . As I_p was ramped up slowly ($dI_p/dt = 0.18 \text{ MA/s}$) a resonance window was found in which ELMs were essentially suppressed, i.e., only isolated large transients between long periods of ELM suppression. The range of q_{95} over which ELMs were suppressed increased when either the current in the C-coil was increased [Figs. 12(b,c,d)] or when the I-coil current was increased [Figs. 12(a,b)]. This distinct window for ELM suppression was seen despite the observation that, after the initial decrease at I-coil turn-on, the pedestal density varied very little during the q -ramp. Detailed analysis of the pedestal profiles from these discharges showed that when ELMs were suppressed by adding additional $n = 1$ perturbation with q_{95} outside the $n = 3$ RMP ELM suppression resonance window, the pedestal pressure and peak pressure gradient were reduced more than for cases with $n = 3$

perturbation within the $n = 3$ q_{95} resonance window that produce complete ELM suppression. So these discharges provide the existence proof that the resonance window for suppression can be increased with combinations of perturbation spectra with different toroidal mode number, but they also show that the degradation of the pedestal performance may be greater when low- n perturbations are used.

The density reduction that is typically seen when the RMP fields are turned on in low collisionality plasmas is not as sensitive to the safety factor as is the complete suppression of the Type-I ELMs. The reduction of the line averaged density and of the pedestal density [Figs. 5(h), 6(f), 7(f), and 12(f)] is similar in discharges for which the I-coil (and C-coil) perturbations are turned on at high q_{95} prior to a q_{95} down ramp [Fig. 12(f)] and for plasmas with lower q_{95} at the turn on time [Figs. 5(h), 6(f), and 7(f)]. In addition, the density can be essentially insensitive to the value of q_{95} during the I_p ramps despite the sharp sensitivity of complete suppression of the ELMs to the safety factor. This suggests that the underlying physics determining the pedestal particle balance response to the RMP (transport and sources) may be different than the physics setting the resonance window for suppression of the ELM instability. In other words, there may be other factors determining the sharp resonance window in q -profile for satisfying P-B stability and achieving complete suppression, besides the change in the pressure profile due to the change in density profile.

IV. DISCUSSION OF THEORY — EXPERIMENT COMPARISON

The correlation of complete ELM suppression, or order of magnitude reduction in maximum ELM size, with a minimum width of the vacuum island overlap region provides a clue to the physics driving the suppression. Another clue is that frequently the largest change in the pressure gradient, between plasmas at low RMP strength that still have ELMs and plasmas with higher RMP strength in which the ELMs are suppressed, occurs in the same region ($0.85 < \Psi_N < 0.9$, i.e., inboard of the steep gradient region) as the inner edge of the island overlap region. Since peeling-ballooning (P-B) stability analysis has shown that when ELMs are suppressed by application of RMPs, the operating point in edge pressure gradient vs edge current density ($\alpha - J$) space is within the stable region, the key to understanding why increased island overlap is correlated with suppression is to understand how overlapping islands in the threshold region $0.85 < \Psi_N < 0.9$ help to move the edge pressure and the corresponding edge bootstrap current from the unstable region (consistent with ELMing) toward the P-B stability boundary. One way to approach this question is to look for differences in the number of magnetic field lines that are lost, from the threshold region to material surfaces due to the RMP, between cases at low RMP strength that are ELMing vs cases at higher RMP strength for which the ELMs are suppressed.

There is a clear increase in both the number of field lines lost and the fraction of the field lines lost with connection length comparable to the electron-ion collisional mean free path (mfp), in cases with ELM suppression compared with similar plasmas at lower RMP strength that do not achieve suppression. Detailed field line tracing indicates that both the increase in field line loss fraction and the increase in the number of field lines

lost with short connection length extends from the plasma edge in to approximately $\Psi_N = 0.85$. The field line tracing calculations were done with the TRIP3D code [60]. A total of 1800 field lines were traced in 10 groups of 180 lines each. The launch locations of the lines in each group were uniformly distributed spatially on a poloidal flux surface from the axisymmetric kinetic equilibrium reconstruction. The 10 groups covered the flux surfaces from $0.75 \leq \Psi_N \leq 0.95$ in steps of $\Delta\Psi_N = 0.02$. The field lines were traced in the forward direction (toward the outer divertor target) until they either hit the target or they completed 200 toroidal revolutions. The full 3D geometry of all the vacuum magnetic fields in the experiment, including those due to the I-coil, the C-coil and the intrinsic error fields was included. A comparison of the field line loss fraction (i.e., the fraction that hit the target in less than 200 revolutions) as a function of the flux surface where they were initially launched, for three of the cases from the I-coil current scan (Fig. 5) is shown in Fig. 13. This analysis shows increases of between 30%-40% in the fractional field line loss over the region $0.85 < \Psi_N < 0.90$ for the two ELM suppressed cases at higher I-coil current (RMP strength) compared with the ELMing case at lower I-coil current. Smaller increases in the fractional field line loss are observed even further into the plasma, although the statistical significance of the difference is marginal due to low sampling rates. The fraction of the field lines that were lost with forward connection length to the outer divertor target less than two electron-ion collisional mean-free-paths (mfps) (Fig. 14) also shows an increase across the region of $0.85 < \Psi_N < 0.95$. Here the local collisional mfp $\lambda_{mfp} = 45.7(T_e^{ped})^2 / (Z_{eff} n_e^{ped} \log \Lambda)$ at the origin of the field line in the pedestal is used for the normalization, where T_e^{ped} and n_e^{ped} are the pedestal electron temperature and density respectively, and $\log \Lambda = 15.2 - 0.5 \log(n_e) + \log(T_e)$ with T_e^{ped} in

keV and n_e^{ped} in 10^{20}m^{-3} . The largest relative increase in the fractional loss of these short field lines is in the region $0.86 < \Psi_N < 0.89$. The change in the fractional loss of field lines with connection length less than 3 or 5 collisional mfps is even more pronounced in the region $0.85 < \Psi_N < 0.90$ (not shown).

These results suggest that changes in the plasma potential in the region $0.85 < \Psi_N < 0.9$ may be playing an important role in the physics processes that move the pedestal operating point inside the stable region of the P-B stability boundary in the ELM suppressed cases. The plasma from this region that is connected to the divertor targets on the short field lines will be at a very different potential than the well confined plasma on nearby field lines that have long (or infinite) connection length. It has been suggested [61-63] that the electric fields generated by such variations in plasma potential could produce $E \times B$ convection cells that might increase the particle transport within the edge plasma. This is at least qualitatively consistent with the observations of reduced plasma pressure gradients, due primarily to reduced density gradients, seen in this region in the ELM suppressed cases. However, work remains to be done to verify that this model is consistent with the observations of pedestal density reductions when the RMP is turned on in plasmas with q -profile outside the resonance window for ELM suppression. Connecting both the insensitivity of the initial pedestal density reduction to the q -profile at RMP turn-on and the subsequent insensitivity of the pedestal density to variations in the q -profile during safety factor ramps, with a model asserting that $E \times B$ convective cells contribute to increased particle transport from inside the top of the pedestal remains a topic for future analysis.

Finally, although work continues on the basic physics driving the suppression of ELMs by RMPs, the simple picture described here can provide guidance to initial studies of candidate coil designs for future tokamaks such as ITER. Recent work surveyed a range of possible RMP coil designs for ELM control in ITER [50]. In this kind of survey the first specification that must be made is the current required in the coils to satisfy a criterion for ELM suppression. From the results reported here, an initial estimate of the required coil currents for the different candidate designs was made based on a criterion that the coils must produce a Chirikov parameter greater than 1.0 from the plasma edge to $\Psi_N = 0.85$. This allowed estimates of the mode spectra of the different designs to be examined and initial estimates of the space necessary for the conductors to carry the estimated currents to be made and discussed [50, 64]. Work to refine these estimates will certainly continue in this area.

V. CONCLUSIONS

ELM suppression was achieved in plasmas with an ISS and pedestal electron collisionality similar to that expected for ITER, $\nu_e^* = 0.1$, for a wide range of $n = 3$ RMP field strength, for a range of combinations of $n = 3$ and $n = 1$ perturbation fields, and for a range of safety factor profiles. The data indicates that full suppression of Type-I ELMs is a resonant phenomenon that depends sensitively on the safety factor profile. The range of q -profiles that achieved full suppression was increased either by increasing the strength of the $n = 3$ RMP fields, or by increasing the strength of $n = 1$ fields only in combination with sufficiently strong $n = 3$ fields.

A simple model that proposes that the maximum ELM size observed would be related to the width of the region in the edge plasma with good overlap of the vacuum magnetic islands, is qualitatively consistent with the data from I-coil current, B_T , and gas puffing scans in plasmas with the ISS and fixed B_T/I_p ratio such that the q -profile was within the resonance window for full ELM suppression. Reduction of the ELM size, measured by D_α signals in the divertor, to less than 5% of the ELM size without RMPs is correlated with vacuum island overlap width in the edge greater than a threshold value. Initial field line tracing calculations using the vacuum fields showed an increase in the number of field lines lost with short connection length to the divertor targets, from the same region as the increase in island overlap in an ELM suppressed case compared with an ELMing case. This may suggest a role for $E \times B$ convection in changing the pedestal profiles in such a way as to satisfy P-B stability and suppress ELMs.

However, the detailed physics understanding of why the maximum ELM size correlates with the width of the island overlap region or the fractional loss of short field

lines using vacuum fields remains for future work. The correlation holds for plasmas with fixed shape and B_T/I_p ratio such that the q -profile was within the resonance window for full ELM suppression, in which the vacuum field RMP strength or the pedestal density is varied. However, in the scans of I_p , at fixed B_T and shape, this correlation is not seen; in these scans the island overlap region width at higher B_T/I_p ratio during the ELMing phase is larger than the overlap width during phases with full ELM suppression in which the B_T/I_p ratio produced a q -profile in the resonance window. In addition, the vacuum island overlap width does not take into account the response of the plasma to the applied fields, including the possible screening of the vacuum fields [65,66] by the effects of plasma rotation. The physics underlying the difference between ELM mitigation (moderate size reduction and frequency increase) due to RMPs and full ELM suppression must be determined by including the self-consistent fields within the plasma, but this analysis is beyond the scope of this paper. The fully self-consistent simulations will likely identify parameters that order the maximum ELM size data at least as well as the vacuum island overlap width, and will also show the physics mechanisms leading to that ordering. However, until those fully self-consistent simulations are available, the model of a minimum vacuum island overlap width required to achieve full ELM suppression provides an initial criterion by which to estimate the required currents in candidate coil designs for future tokamaks including ITER, and then to begin to evaluate the additional consequences, on other aspects of plasma operation, of applying perturbations of the estimated required size.

Acknowledgment

This work was performed under the auspices of the U.S. Department of Energy by Lawrence Livermore National Laboratory in part under Contract W-7405-Eng-48 and in part under Contract DE-AC52-07NA27344, and under DE-FC02-04ER54698, DE-FG02-07ER54917 and DE-FG02-05ER54809.

References (Woodie, Todd thinks the rule for Phys Plasmas is (a) if 5 or fewer authors then list all of them, (b) if more than 5 authors then list 3 and add et al. Can you confirm that this is the rule and if so reduce the long author lists below. If this is the rule then I will eventually have to look up a bunch of authors for the references with short lists – ugh!)

1. G. Federici, P. Andrew, P. Barabaschi, J. Brooks, R. Doerner, A. Geier, A. Herrmann, G. Janeschitz, K. Krieger, *et al.*, J. Nucl. Mater. **313-316**, 11 (2003).
2. S. C. Cowley, *et al.*, Plasma Phys. Control. Fusion **45**, A31 (2003); H. R. Wilson and S. C. Cowley, Phys. Rev. Lett. **92**, 175006 (2004).
3. A. W. Leonard, J. A. Boedo, M. E. Fenstermacher, R. J. Groebner, M. Groth, C. J. Lasnier, M. A. Mahdavi, T. H. Osborne, D. L. Rudakov, *et al.*, J. Nucl. Mater. **313-316**, 768 (2003). (20% of pedestal energy lost)
4. ITER Physics Basis Editors, “ITER Physics Basis,” Nucl. Fusion **39**, 2137 (1999); ITER Physics Basis Editors, “Progress on the ITER Physics Basis,” accepted for publication in Nucl. Fusion (2007).
5. A. Zhitlukhin *et al.*, J. Nucl. Mater. **363-365**, 301 (2007).
6. H. Zohm, Plasma Phys. Control. Fusion **38**, 105 (1996).
7. M. E. Fenstermacher, A. W. Leonard, P. B. Snyder, J. A. Boedo, N. H. Brooks, R. J. Colchin, D. S. Gray, R. J. Groebner, M. Groth, *et al.*, Plasma Phys. Control. Fusion **45**, 1597 (2003).
8. P. T. Lang, G. D. Conway, T. Eich, L. Fattorini, O. Gruber, S. Günter, L. D. Horton, S. Kalvin, A. Kallenbach, *et al.*, Nucl. Fusion **44**, 665 (2004).

9. A. W. Degeling, Y. R. Martin, J. B. Lister, L. Villard, V. N. Dokouka, V. E. Lukash, and R. R. Khayrutdinov, *Plasma Phys. Control. Fusion* **45**, 1637 (2003).
10. P. T. Lang, A. W. Degeling, J. B. Lister, Y. R. Martin, P. J. McCarthy, A. C. C. Sips, W. Suttrop, G. D. Conway, L. Fattorini, *et al.*, *Plasma Phys. Control. Fusion* **46**, L31 (2004).
11. Y. Kamada, R. Yoshino, Y. Neyatani, M. Sato, S. Tokuda, A. Azumi, S. Takeji, K. Ushigusa, T. Fukuda, *et al.*, *Plasma Phys. Control. Fusion* **38**, 1387 (1996).
12. J. Stober, O. Gruber, A. Kallenbach, V. Mertens, F. Ryter, A. Stabler, W. Suttrop, W. Treutterer, and the ASDEX Upgrade Team, *Plasma Phys. Control. Fusion* **42**, A211 (2000).
13. R. Maingi, K. Tritz, E. D. Fredrickson, J. E. Menard, S. A. Sabbagh, D. Stutman, M. G. Bell, R. E. Bell, C. E. Bush, *et al.*, *Nucl. Fusion* **45**, 264 (2005).
14. R. Maingi, C. E. Bush, E. D. Fredrickson, D. A. Gates, S. M. Kaye, B. P. LeBlanc, J. E. Menard, H. Meyer, D. Mueller, *et al.*, *Nucl. Fusion* **45**, 1066 (2005).
15. G. Saibene, P. J. Lomas, R. Sartori, A. Loarte, J. Stober, Y. Andrew, S. A. Arshad, G. D. Conway, E. de la Luna, *et al.*, *Nucl. Fusion* **45**, 297 (2005).
16. Y. Takase, R. L. Boivin, F. Bombada, P. T. Bonoli, C. Christensen, C. Fiore, D. Garnier, J. A. Goetz, S. . Golovato, *et al.*, *Phys. Plasmas* **4**, 1647 (1997).
17. K. Kamiya, H. Kimura, H. gawa, H. Kawashima, K. Tsuzuki, M. Sato, Y. Miura, and JFT-2M Group, *Nucl. Fusion* **43**, 1214 (2003).
18. T. Ozeki, *et al.* *Nucl. Fusion* **30** (1990) 1425.

19. K. H. Burrell, M. E. Austin, D. P. Brennan, J. C. DeBoo, E. J. Doyle, C. Fenzi, C. Fuchs, P. Gohil, C. M. Greenfield, *et al.*, Phys. Plasmas **8**, 2153 (2001).
20. K. H. Burrell, W. P. West, E. J. Doyle, M. E. Austin, J. S. deGrassie, P. Gohil, C. M. Greenfield, R. J. Groebner, R. Jayakumar, *et al.*, Plasma Phys. Control. Fusion **46**, A165 (2004).
21. W. Suttrop, G. D. Conway, L. Fattorini, L. D. Horton, T. Kurki-Suonio, C. F. Maggi, M. Maraschek, H. Meister, R. Neu, *et al.*, Plasma Phys. Control. Fusion **46**, A151 (2004).
22. Y. Sakamoto, H. Shirai, T. Fujita, S. Ide, T. Takizuka, N. Oyama, and Y. Kamada, Plasma Phys. Control. Fusion **46**, A299 (2004).
23. W. P. West, K. H. Burrell, T. A. Casper, E. J. Doyle, P. B. Snyder, P. Gohil, L. L. Lao, C. J. Lasnier, A. W. Leonard, *et al.*, Nucl. Fusion **45**, 1708 (2005).
24. J.S. DeGrassie, N. Ohya, N.H. Brooks *et al.*, J. Nucl. Mater. **128-129**, 266 (1984)
25. T.E. Evans, J.S. DeGrassie, G.L. Jackson *et al.*, J. Nucl. Mater., **145-147**, 812 (1987)
26. S.C. McCool, A.J. Wooton, A.Y. Aydemir *et al.*, Nucl. Fusion, **29** 547 (1989).
27. A.J. Wooton, J. Nucl. Mater., **176-177**, 77 (1990).
28. S.C. McCool, A.J. Wooton, M. Kottschenreuther, *et al.*, Nucl. Fusion **30** 167 (1990)
29. Ph. Ghendrih, A. Grossman, and H. Capes, Plasma Phys. Control. Fusion **38**, 1653 (1996).

30. Ph. Ghendrih, M. Bécoulet, L. Colas, A. Grosman, R. Guirlet, J. Gunn, T. Loarer, A. Azéroual, V. Basiuk, *et al.*, Nucl. Fusion **42**, 1221 (2002).
31. K. H. Finken, G. Fuchs, B. Glesen, M. Haßler, R. Koch, G. Mank, A. Nicolai, A. Rogister, M. Z. Tokar, *et al.*, J. Nucl. Mater. **220-222**, 448 (1995).
32. K. H. Finken, S. S. Abdullaev, W. Biel, M. F. M. de Bock, C. Busch, E. Farshi, M. von Hellermann, G. M. D. Hogeweij, M. Jakubowski, *et al.*, Plasma Phys. Control. Fusion **46**, B143 (2004).
33. R. C. Wolf, W. Biel, M. F. M. de Bock, K. H. Finken, S. Gunter, G. M. D. Hogeweij, S. Jachmich, M. W. Jakubowski, R. J. E. Jaspers, *et al.*, Nucl. Fusion **45**, 1700 (2005).
34. M. W. Jakubowski, S. S. Abdullaev, K. H. Finken, and the TEXTOR Team, Nucl. Fusion **44**, S1 (2004).
35. K.H. Finken, Nucl. Fusion **46**, S107 (2006).
36. Y. Liang, H. R. Koslowski, P. R. Thomas, E. Nardon, B. Alper, P. Andrew, Y. Andrew, G. Amoux, Y. Baranov, *et al.*, Phys. Rev. Lett. **98**, 265004 (2007).
37. T. E. Evans, M. E. Fenstermacher, R. A. Moyer, T. H. Osborne, J. G. Watkins, P. Gohil, I. Joseph, M. J. Schaffer, *et al.*, “RMP ELM Suppression in DIII-D Plasmas With ITER Similar Shapes and Collisionalities,” accepted for publication in Nucl. Fusion (2007).
38. T.H. Osborne *et al.*, “Edge Stability Analysis and Pedestal and ELM Characteristics in I-coil ELM Suppressed Discharges on DIII-D,” Proc. 32nd EPS Conf. on Controlled Fusion and Plasma Physics, Tarragona, Spain, Vol. 29C (European Physical Society, 2005) Paper P-4.012.

39. K. H. Burrell, T. E. Evans, E. J. Doyle, M. E. Fenstermacher, R. J. Groebner, A. W. Leonard, R. A. Moyer, T. H. Osborne, M. J. Schaffer, *et al.*, Plasma Phys. Control. Fusion **47**, B37 (2005).
40. T. E. Evans, K. H. Burrell, M. E. Fenstermacher, R. A. Moyer, T. H. Osborne, M. J. Schaffer, W. P. West, L. W. Yan, J. A. Boedo, *et al.*, Phys. Plasmas **13**, 056121 (2006).
41. R. A. Moyer, K. H. Burrell, T. E. Evans, M. E. Fenstermacher, I. Joseph, T. H. Osborne, M. J. Schaffer, P. B. Snyder, J. G. Watkins, *et al.*, Proc. of the 49th IAEA Fusion Energy Conf., Chengdu, China (2006).
42. M. E. Fenstermacher, T. E. Evans, R. A. Moyer, G. D. Porter, J. A. Boedo, K. H. Burrell, M. Groth, I. Joseph, T. H. Osborne, and J. G. Watkins, J. Nucl. Mater. **363-365**, 476 (2007).
43. T. E. Evans, R. A. Moyer, P. R. Thomas, J. G. Watkins, T. H. Osborne, J. A. Boedo, E. J. Doyle, M. E. Fenstermacher, K. H. Finken, *et al.*, Phys. Rev. Lett. **92**, 235003 (2004).
44. T. E. Evans and R. A. Moyer, J. Nucl. Mater. **337-339**, 691 (2005).
45. R. A. Moyer, T. E. Evans, T. H. Osborne, P. R. Thomas, M. Becoulet, J. Harris, K.- *et al.*, Phys. Plasmas **12**, 056119 (2005).
46. T. E. Evans, R. A. Moyer, J. G. Watkins, T. H. Osborne, P. R. Thomas, M. Becoulet, J. A. Boedo, E. J. Doyle, M. E. Fenstermacher, *et al.*, Nucl. Fusion **45**, 595 (2005).

47. T. E. Evans, R. A. Moyer, K. H. Burrell, M. E. Fenstermacher, I. Joseph, A. W. Leonard, T. H. Osborne, G. D. Porter, M. J. Schaffer, *et al.*, *Nature Physics* **2**, 419 (2006).
48. P. B. Snyder, H. R. Wilson, J. R. Ferron, L. L. Lao, A. W. Leonard, D. Mossessian, M. Murakami, T. H. Osborne, A. D. Turnbull, and X. Q. Xu, *Nucl. Fusion* **44**, 320 (2004).
49. O. Sauter, C. Angioni, and Y. R. Lin-Liu, *Phys. Plasmas* **6**, 2834 (1999).
50. M. J. Schaffer, J. E. Menard, M. P. Aldan, J. M. Bialek, T. E. Evans, and R. A. Moyer, "Study of In-vessel Non-axisymmetric ELM-suppression Coil Concepts for ITER," Proceedings of the 2007 SFP Workshop, Juelich, Germany, accepted for publication in *Nucl. Fusion* (2007).
51. B. V. Chirikov, *Phys. Reports* **52**, 263 (1979).
52. M. J. Schaffer and R. J. LaHaye, private communication (2007).
53. H. R. Wilson, P. B. Snyder, G. T. A. Huysmans, and R. L. Miller, *Phys. Plasmas* **9**, 1277 (2002).
54. P. B. Snyder, H. R. Wilson, and X. Q. Xu, *Phys. Plasmas* **12**, 056115 (2005);
P. B. Snyder, H. R. Wilson, J. R. Ferron, L. L. Lao, A. W. Leonard, T. H. Osborne, A. D. Turnbull, D. Mossessian, M. Murakami, X. Q. Xu, *Phys. Plasmas* **9** (2002) 2037.
55. P. B. Snyder, K. H. Burrell, H. R. Wilson, M. S. Chu, M. E. Fenstermacher, A. W. Leonard, R. A. Moyer, T. H. Osborne, M. Umansky, *et al.*, *Nucl. Fusion* **47**, 961 (2007).
56. T. H. Osborne, private communication (2007).

57. G. D. Porter, J. Moller, M. Brown, and C. Lasnier, Phys. Plasmas **5**, 1410 (1998).
58. L. L. Lao, **et al.**, Nucl. Fusion **30**, 1035 (1990).
- 59.** J. L. Luxon, M. J. Schaffer, G. L. Jackson, J. A. Leuer, A. Nagy, J. T. Scoville, and E. J. Strait, Nucl. Fusion **43**, 1813 (2003).
60. T. E. Evans, R. A. Moyer, and P. Monet, Phys. Plasmas **3**, 4957 (2002).
61. T. E. Evans, J. S. deGrassie, G. L. Jackson *et al.*, Proc. of 14th EPS Conf. on Controlled Fusion and Plasma Physics, Madrid, Spain, Vol. 11D (European Physical Society, 1987) p. 770.
62. S. Takamura, N. Ohnishi, H. Yourada and T. Okuda, Phys. Fluids **30**, 144 (1987).
63. A. J. Wootton, J. Nucl. Mater. **176-177**, 77 (1990).
64. R. J. Hawryluk and members of ITER Design Review WG1 Design Requirements and Physics Objectives Sub-group on ELM and RWM Control, private communication (2007).
65. R. Fitzpatrick, Phys. Plasmas **5**, 3325 (1998).
66. A. Boozer, Phys. Plasmas **12**, 0925404 (2005).

Table 1. Systems parameters for the five parametric scans considered in this paper.

Scan	Parity	$I_{\text{I-coil}}$ (kA)	C-coil Multiplier	I_{p} (MA)	B_{T} (T)	q_{95}	Gas (Tl/s)
I-coil current	Even	0-6.3	1.0	1.68	2.14	3.60	0
$\delta br/B_{\text{T}}$	Even	5.8	1.0	1.4-1.68	1.77-2.14	3.60	0
$n_{\text{e}}^{\text{ped}}$	Even	4.0	1.0	1.55	1.93	3.53	0.85, 2.20
High q_{95}	Odd	0, 5.5, 6.3	1.0	0.81-0.93	1.93	6.30, 7.50	0
$n = 3 + n = 1$ in q -scan	Even	3.0, 4.0	1.0, 1.2, 2.0	1.34-1.70	1.93	3.25-4.18	0

Figure Captions

Fig. 1. Plasma and coil geometry including (a) high triangularity ISS showing the optimal position of the outer strike point for pumping, the location of the gas injection used in the pedestal density scan, the location of the D_α line integrated measurement used to estimate the ELM size, and the locations of the I- and C-coils, and (b) 3D rendering of the I-coil and C-coil geometry.

Fig. 2. Time histories of plasma parameters for a typical ELM suppression discharges showing (a) outer divertor D_α intensity (1×10^{13} phot/cm²/s/str), (b) I-coil current (kA), (c) pedestal electron collisionality, ν_e^* , from [49], (d) confinement factor $H(98,y2)$ from [4], (e) pedestal electron density (10^{19} m⁻³), (f) pedestal electron temperature (keV), and (g) toroidal rotation near the top of the pedestal (km/s).

Fig. 3. Contours of poloidal mode spectrum of $n = 3$ perturbation from the I-coils configured with even parity as a function of poloidal mode number and normalized poloidal flux in the plasma. For oppositely directed B_T and I_p in DIII-D, resonant modes from the I-coil have negative poloidal mode number. Pitch resonant modes with $m = -nq(\Psi_N)$ are shown by the blue dashed line.

Fig. 4. Radial profiles of magnetic and plasma parameters at 2500 ms in the plasma of Fig. 2 including the structure of the magnetic islands from the I-coil ($n = 3$, red), C-coil ($n = 1$, black) and intrinsic error fields ($n = 2$, green and contributions to $n = 1,3$) aligned in pitch resonance with the experimental q -profile. Also shown are the profile of the calculated Chirikov parameter and the fit used to determine the width of the region with

Chirikov parameter >1.0 . Vertical dashed lines indicate separatrix of axisymmetric equilibrium ($\Psi_N = 1$) and location of Chirikov parameter $=1.0$ from the fit ($\Psi_N = 0.83$). Profiles of the total plasma pressure, the gradient of total plasma pressure, and the corresponding edge parallel current (including the bootstrap current contribution) are shown for comparison. The edge pressure pedestal is shown by the shaded region.

Fig. 5. Time histories of multiple discharges in the scan of I-coil current, showing (a-f) D_α intensity (10^{13} photons/cm²/s/str), for each discharge, and (g) pedestal electron density (10^{19} m⁻³). I-coil current and $\delta b_r^{11/3}/B_T$ are (a) 0 kA, 0, (b) 4.0 kA, 3.0×10^{-4} , (c) 4.8 kA, 3.7×10^{-4} , (d) 5.3 kA, 4.0×10^{-4} , (e) 5.7 kA, 4.4×10^{-4} , (f) 6.3 kA, 4.9×10^{-4} . I-coil turn-on indicated by green dashed line.

Fig. 6. Time histories of multiple discharges in the scan of $\delta b_r/B_T$ at constant B_T/I_p , showing (a-c) D_α intensity (10^{13} photons/cm²/s/str), for each discharge, (d) I_p (MA), and (e) pedestal electron density (10^{19} m⁻³). I-coil current = 5.7 kA. B_T and $\delta b_r^{11/3}/B_T$ is (a) 2.14 T and 4.4×10^{-4} , (b) 1.95 T and 4.7×10^{-4} , (c) 1.75 T and 5.3×10^{-4} . I-coil turn-on indicated by green dashed line.

Fig. 7. Time histories of multiple discharges in the scan of pedestal pressure by gas puffing, showing (a-d) D_α intensity (10^{13} photons/cm²/s/str), for each discharge, (e) pedestal electron pressure, (f) pedestal electron density (10^{19} m⁻³), and (g) pedestal electron temperature (keV). Time average gas injection rates were (a) 0.85 TL/s, (b), (c), (d) 2.2 TL/s. I-coil turn-on indicated by green dashed line.

Fig. 8. Peak magnitude of ELM transient on outer strikepoint D_α signal as a function of the width in normalized flux of the vacuum island overlap region with Chirikov parameter >1.0 ($\Delta_{\text{chir}>1}$) for multiple transients in the discharges from Figs. 6, 7, and 8. (a) The value of ELM size plotted is normalized to the maximum size of the ELMs in the H-mode phase prior to application of the I-coil RMP field, (b) plot expanded for timeslices with the RMP coil on.

Fig. 9. Time histories of parameters from two similar discharges (black and red) with I_p up ramps (q_{95} down ramps) used to identify the q -window for ELM suppression with $n = 3$ RMPs from the I-coil, including (a) I_p (MA) and injected neutral beam power P_{nb} (MW), (b) I-coil and C-coil currents (kA), (c) q_{95} and q_0 (q on axis) from standard EFITs, (d) pedestal electron density (10^{19} m^{-3}), (e,f) outer divertor D_α intensity ($10^{13} \text{ photons/cm}^2/\text{s/str}$), (g) amplitude of odd toroidal mode number core MHD activity, (h) amplitude of even toroidal mode number core MHD activity. Shaded regions indicate periods of ELM suppression.

Fig. 10. Contours of poloidal mode spectrum of $n = 3$ perturbation from the I-coils configured with odd parity as a function of poloidal mode number and normalized poloidal flux in the plasma. For oppositely directed B_T and I_p in DIII-D, resonant modes from the I-coil have negative poloidal mode number. Pitch resonant modes with $m = -nq(\Psi_N)$ are shown by the white dashed line.

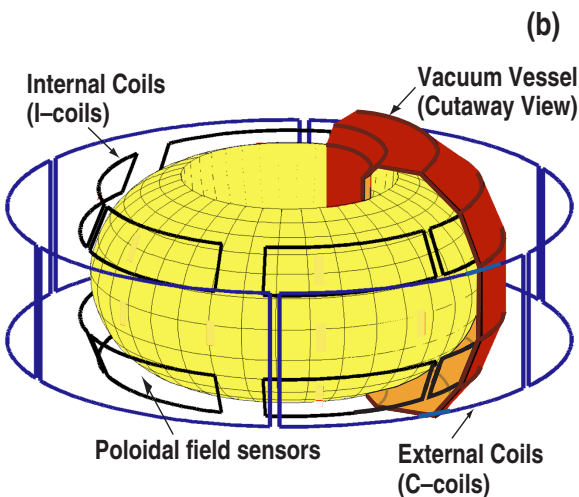
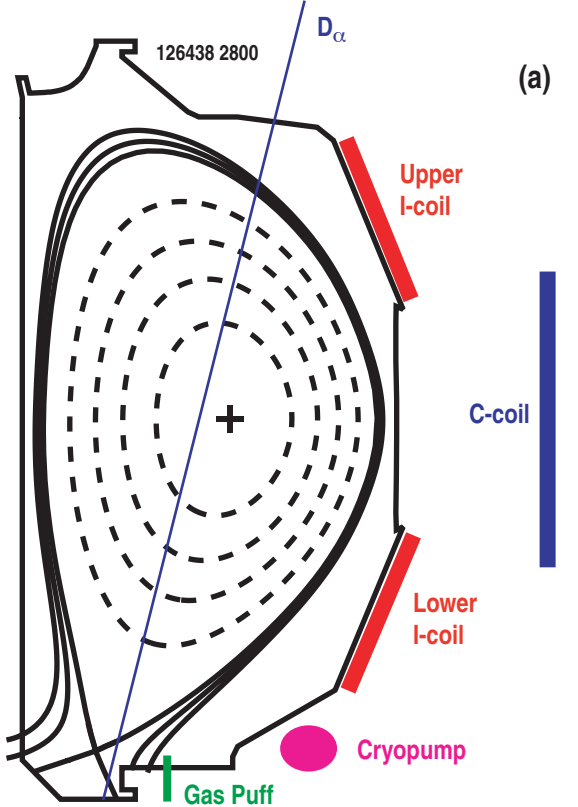
Fig. 11. Time histories of parameters from discharges at high $q_{95} = 7.5$ with odd parity, $n = 3$ RMPs from the I-coil, including (a-c) D_α intensity ($10^{13} \text{ photons/cm}^2/\text{s/str}$), for

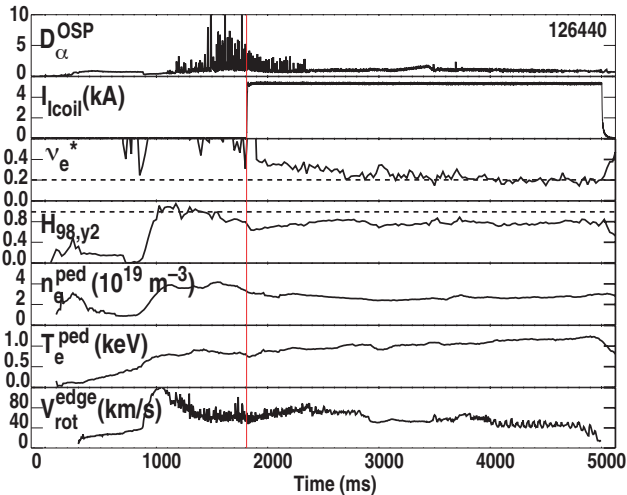
each discharge, (d) pedestal electron density (10^{19} m^{-3}). I-coil current, q_{95} and $\delta b_r^{11/3}/B_T$ are (a) 0 kA, 7.5, 0, (b) 5.7 kA, 6.2, 0.70×10^{-4} , (c) 6.3 kA, 7.5, 0.78×10^{-4} . I-coil turn-on time indicated by green dashed line.

Fig. 12. Time histories of parameters from discharges with different combinations of $n = 3$ RMP from the I-coil and $n = 1$ perturbation from the C-coil, including (a-c) D_α intensity ($10^{13} \text{ photons/cm}^2/\text{s/str}$), for each discharge, (d) q_{95} from standard EFITs, (e) pedestal electron density (10^{19} m^{-3}). I-coil current, $\delta b_r^{11/3}/B_T$, and C-coil current are (a) = 4.0 kAt, 3.2×10^{-4} , 9.6 kAt, (b) 3.0 kAt, 2.5×10^{-4} , 9.6 kAt, (c) 3.0 kAt, 2.5×10^{-4} , 4.8 kAt. I-coil turn-on time indicated by green dashed line.

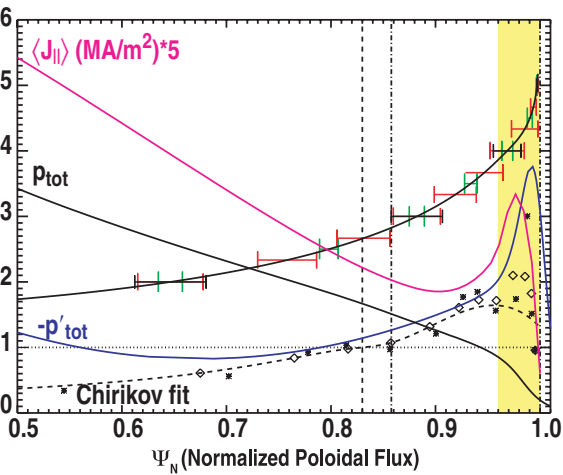
Fig. 13. Results from the field line tracing calculations as functions of normalized poloidal flux for the 4.0 kAt (black), 5.3 kAt (green) and 5.7 kAt (red) cases in the I-coil current scan (D_α traces in Figs. 5b,d,e), showing fraction of field lines that strike the outer divertor target.

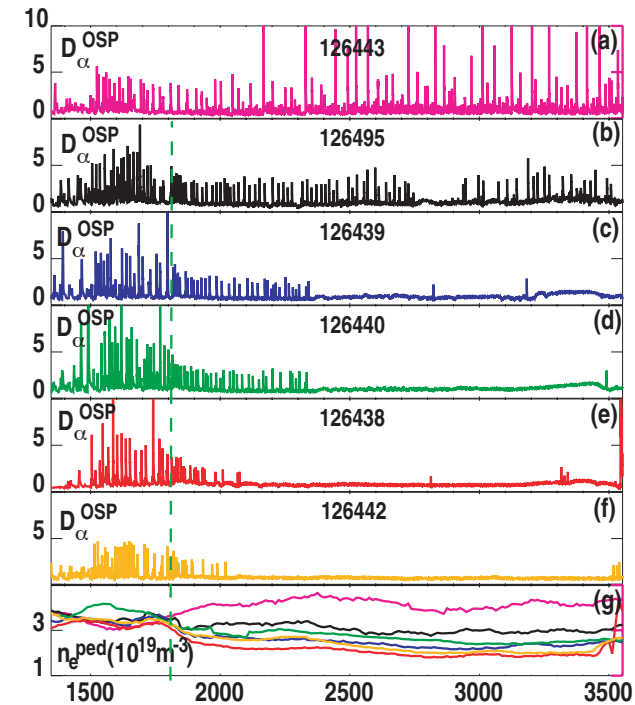
Fig. 14. Fraction of field lines lost to the outer divertor target with connection length less than two electron-ion mean free path lengths for the three discharges of Fig. 13.

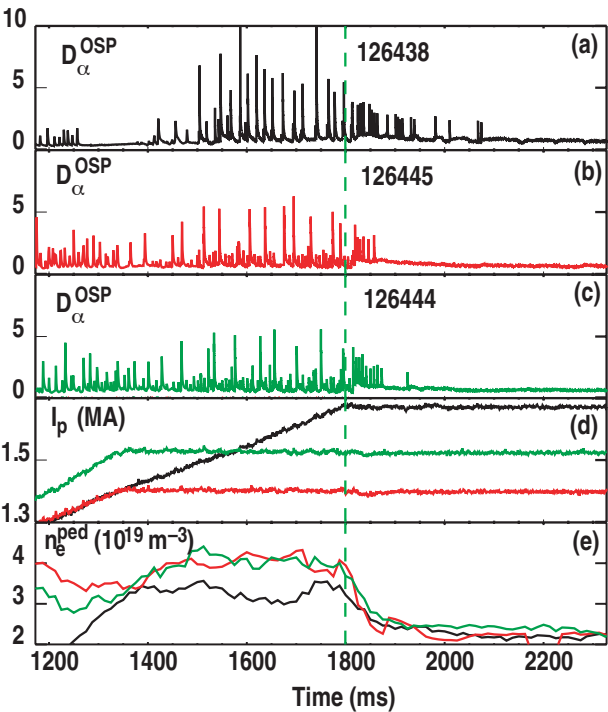


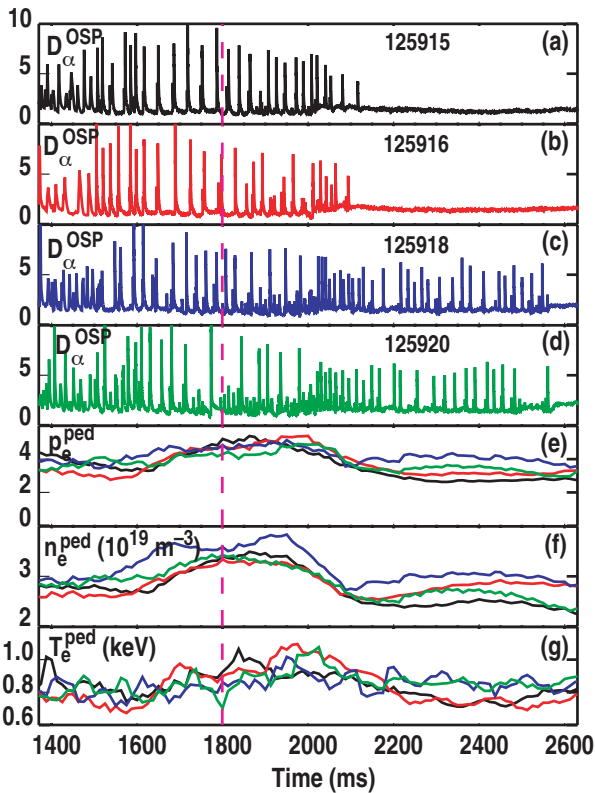


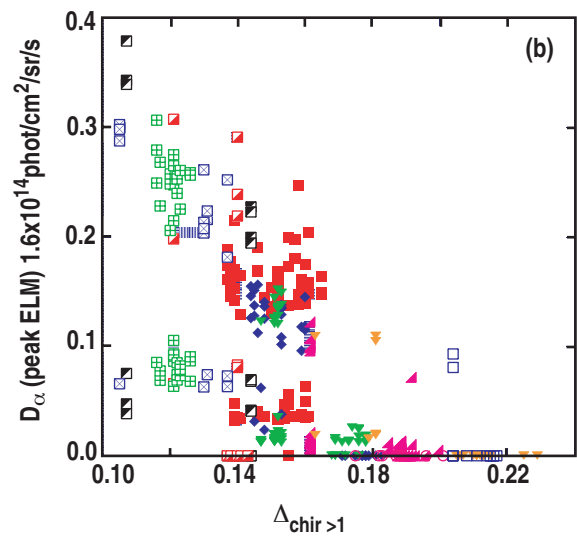
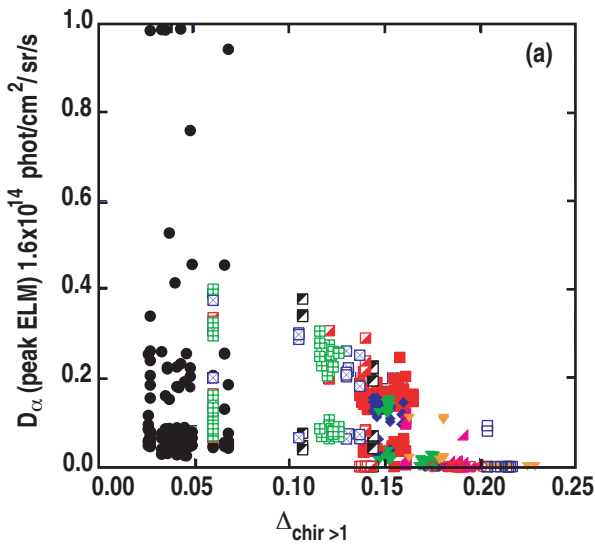


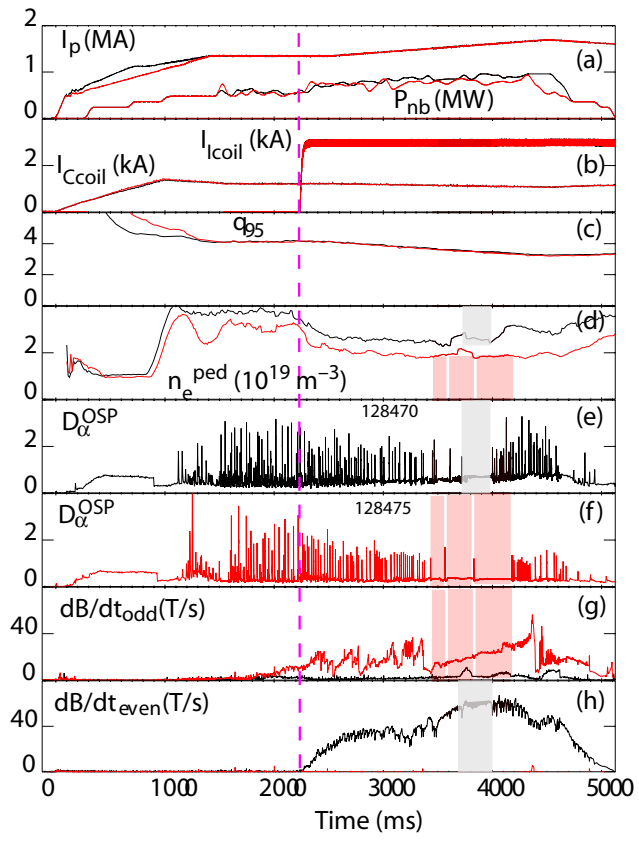




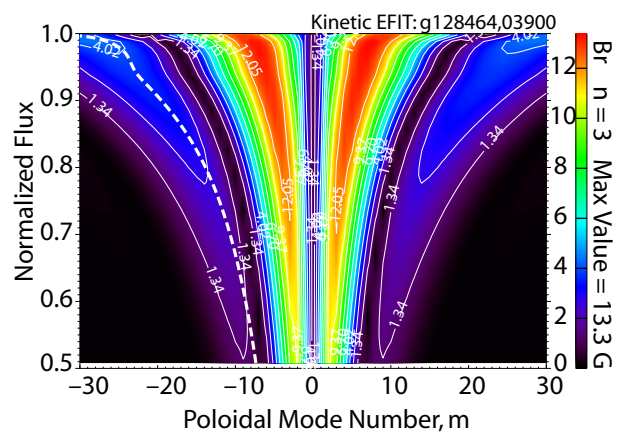








221-07 fig.9 jy



221-07 fig. 10 jy

